# Removing Atmospheric Noise from InSAR Interferograms in Mountainous Regions with a Convolutional Neural Network

George Brencher, Scott T. Henderson, and David E. Shean

***Abstract*—Atmospheric errors in interferometric synthetic aperture radar (InSAR)-derived estimates of surface deformation often obscure real displacement signals, especially in mountainous regions. As climate change disproportionately impacts the mountain cryosphere, developing a technique for atmospheric correction that performs well in high-relief terrain is increasingly important. Here, we developed and implemented a statistical machine learning-based atmospheric correction that relies on the differing spatial and topographic characteristics of periglacial features and atmospheric noise. Our correction is applied at the native spatial and temporal resolution of the InSAR data (40 m, 12 days), does not require external atmospheric data, and can correct both stratified and turbulent atmospheric noise. Using Sentinel-1 data from 2015-2022, we trained a convolutional neural network (CNN) on atmospheric noise from 136 short-baseline interferograms and displacement signals from time-series inversion of 337 interferograms. The CNN correction was then tested on a densely connected network of 202 Sentinel-1 interferograms which were inverted to create a displacement time series. We used the Rocky Mountains in Colorado as our training, validation, and testing areas. When applied to our validation data, our correction offers a 690% improvement in performance over a global meteorological reanalysis-based correction and a 209% improvement over a high-pass filter correction. We found that our correction reveals previously hidden time-dependent kinematic behavior of three representative rock glaciers in our testing dataset. Our flexible, robust approach can be used to correct arbitrary InSAR data to analyze subtle surface deformation signals for a range of science and engineering applications.**

***Index Terms*—Atmospheric correction, machine learning, artificial neural network, regression, interferometry, cryosphere, permafrost, rock glacier**

## I. INTRODUCTION

Interferometric synthetic aperture radar (InSAR) is a remote sensing technique that can be used to measure millimeter-scale deformation of the Earth's surface from space [1]. This sensitivity makes InSAR a powerful tool for deformation monitoring with an array of applications in Earth science and engineering disciplines [2], [3]. However, noise caused by interaction of the radar signal with the atmosphere limits the accuracy of InSAR-derived surface displacement maps [4]. Atmospheric noise is especially detrimental in mountainous regions, where high-relief topography causes atmospheric turbulence and strong variation in relative humidity over short spatial and temporal scales. This situation is further exacerbated by limited availability of validation data, restricted snow-free observation periods, and poor options for reliable stable reference points [5]–[7]. Along with issues caused by steep slopes, including layover and radar shadow [8]–[10] atmospheric noise makes effective processing and interpretation of InSAR data challenging in mountain environments.

As climate change disproportionately impacts the mountain cryosphere [11], an atmospheric correction for InSAR data that performs well in mountainous regions is increasingly necessary to accurately monitor and understand changing natural hazards and water resources. Such a correction would provide insight into the changing deformation regime of glaciers [12], permafrost [13], ice-cored moraines [14], and landslides [15]. At the same time, large quantities of archived SAR data, on-demand InSAR processing, and cloud-computing resources for machine learning provide opportunities for new methods to correct atmospheric noise. A statistical learning approach can take advantage of large data archives to remove stratified and turbulent atmospheric noise from individual interferograms in mountainous regions. This approach relies on the fact that atmospheric noise has different spatial and topographic characteristics than signals related to displacement of alpine permafrost features.

As radar signals travel through the spatially heterogeneous atmosphere, their velocity is slightly altered. Changing temperature, pressure, and relative humidity modulate the refractive index, causing a two-way phase delay in the radar echo [4]. At C-band wavelengths (~5.5 cm), most of this delay occurs in the lower 5 km of the troposphere, where water vapor partial pressure is highest [16], [17]. Tropospheric conditions change significantly on sub-hourly time-scales, causing differing two-way phase delays during successive radar acquisitions and introducing an atmospheric component into the interferometric phase offset [17], [18]. This offset manifests as

G.B. was supported by NSF GRFP DGe-2140004. D.S. was supported by NASA award 80NSSC22K1094.

George Brencher is with the Civil and Environmental Engineering Department, University of Washington, Seattle, WA 98195 USA (e-mail: gbrench@uw.edu)

Scott T. Henderson is with the Department of Earth and Space Sciences and the eScience Institute, University of Washington, Seattle, WA 98195 USA (e-mail: scottyh@uw.edu)

David E. Shean is with the Civil and Environmental Engineering Department, University of Washington, Seattle, WA 98195 USA (e-mail: dshean@uw.edu)

apparent displacement signals of up to 15-20 cm in magnitude, with spatial wavelengths ranging from short (km) to longer scale (tens of km) that are unrelated to deformation of the ground surface [16], [19]–[21]. Atmospheric noise is typically described as 'stratified' or 'turbulent,' depending on its physical origin. Stratified atmospheric noise is caused by coherent changes in altitude-correlated gradients of pressure, temperature, and water vapor; it typically manifests as elevation-dependent noise and is prominent in mountainous regions [16], [17]. Turbulent atmospheric noise is caused by turbulent mixing of water vapor in the lower troposphere, and typically manifests as km-scale noise [16], [17]. A third noise component results from landscape-scale lateral changes in temperature, pressure and water vapor, and manifests as gradual phase gradients over tens of kilometers [16]. Li et al. [20] found that a spatial resolution of 0.3 km was required to characterize and remove 90% of atmospheric noise in C-band interferograms over the Shanghai region in China, which is mostly flat. Higher spatial resolutions (<300 m) are likely required where rugged topography shortens noise length scales.

### *A. Atmospheric Noise Correction: Previous work*

Atmospheric noise corrections can be broken into two groups – those that rely on external atmospheric data and phase-based methods that characterize noise empirically. Typical sources of atmospheric data used for interferogram correction include ground-based meteorological observations [5], [22], path delays from fixed global navigation satellite systems (GNSS) reference stations [23]–[25], global meteorological reanalysis data [26]–[28], regional atmospheric models [29], [30], and near-infrared water vapor products from spaceborne spectrometers (e.g. Moderate Resolution Imaging Spectroradiometer (MODIS) [31], Medium Resolution Imaging Spectrometer (MERIS) [32]).

Below, we briefly consider some limitations of existing atmospheric correction techniques relevant to application in mountainous regions. GNSS and meteorological stations provide point estimates of differential phase delay which require interpolation to produce noise maps at typical InSAR resolutions (<100 m). In mountainous regions where GNSS and meteorological stations are sparse, even sophisticated interpolation likely misses most short-scale turbulent noise. Global meteorological reanalysis data products typically have spatial resolutions of tens of kilometers, requiring downscaling to typical InSAR resolutions and producing mixed correction results in high-relief terrain. Both global and regional atmospheric models may have reduced accuracy in mountain regions where there is a dearth of accurate in-situ meteorological data [33]–[35]. Furthermore, the temporal resolution of most climate model outputs (typically 1 or 6 hour intervals) may not align well with SAR satellite acquisition timestamps, potentially requiring temporal interpolation and further reducing correction accuracy [36]. Corrections derived from optical spectrometers (e.g., MERIS, MODIS) also suffer from relatively coarse (~1 km) spatial resolution and relative acquisition time issues, with the added requirement of solar illumination and cloud-free conditions. While spectrometers provide water vapor products, they cannot be used to correct for atmospheric noise caused by variable pressure and temperature, which is non-negligible in mountainous terrain [17].

Empirical methods to correct atmospheric noise use linear, piecewise, and power-law relationships between surface elevation and phase to remove elevation-dependent noise [37], [38]. Interferogram stacking [4], [39] is a simple method to derive mean surface displacement from multiple interferograms, canceling random atmospheric noise that is not spatially or temporally correlated. However, stacking is not a viable correction option for a limited number of interferograms or where surface deformation occurs on short timescales relative to the observation interval. Zebker [40] demonstrated an approach that uses multiple reference points to remove noise from a single interferogram. While promising, this approach is computationally intensive and may be ineffective for large-area displacements or where coherence is low in the vicinity of features of interest, as is frequently the case in mountainous terrain. Despite more than two decades of research, mitigation of atmospheric noise remains a significant challenge, with no universal approach for mountainous regions [21].

### *B. Atmospheric Noise Correction with Machine Learning*

Where displacement signals of interest have different spatial and/or temporal characteristics than co-occurring atmospheric noise, convolutional neural networks (CNNs) present an alternative option for atmospheric noise correction that can address many of the limitations of existing methods. CNNs are a central tool in computer vision and are frequently applied to image denoising problems [41]–[43]. Through a series of convolutions and pooling operations, CNNs restructure images to create simplified latent representations of patterns in the data. These representations can then be expanded to the input dimensions, retaining only selected characteristics of the original image. In the field of InSAR processing, CNNs have previously been used to filter wrapped interferograms [44]–[46], to unwrap interferograms [47]–[49], and to detect deformation related to ground subsidence [50], [51], volcanic activity [52], [53], mining [47], [54], landslides [55], and earthquakes [56]. Chen et al. [57] implemented a multi-layer perceptron neural network to remove elevation-dependent atmospheric noise from interferograms. Rouet-Leduc et al. [58] used a CNN to extract cumulative displacement related to fault activity from short interferogram time series, relying on spatiotemporal differences in atmospheric noise and displacement signals of interest. While effective, this approach is analogous to an improved method of interferogram stacking, and like interferogram stacking, it ultimately results in a single reduced measurement from multiple observations.

Here, we present a CNN atmospheric correction based solely on the differing spatial and topographic characteristics of atmospheric noise and displacement signals of interest. Our correction is applied at the native spatial and temporal resolution of the original InSAR data. It does not rely on external atmospheric data or synthetic training data, and it can remove both stratified and turbulent atmospheric noise in mountainous terrain. We developed and tested our approach using publicly available SAR data, on-demand InSAR processing services, cloud-based machine learning resources, and open-source software.

## II. DATA AND STUDY SITE

### *A. Data*

We used Copernicus Sentinel-1 C-band single-look complex (SLC) radar data collected between June 15 and October 15 during the period from 2015 to 2022. Data were acquired in interferometric wide (IW) swath mode (250-km swath width) with vertical co-polarization (VV) along ascending (satellite moving north and looking east) relative orbits 151 and 49 and descending (satellite moving south and looking west) relative orbit 56. The Sentinel-1 SLCs have a spatial resolution of 22 m in azimuth (i.e., along-track direction) and 2.7-3.5 m in range (i.e., across-track direction) depending on incidence angle. Minimum revisit times vary between 6 and 12 days. Interferograms were processed using the Alaska Satellite Facility's Hybrid Pluggable Processing Pipeline (ASF HyP3) [59]. We performed multi-looking (10 looks in range and 2 looks in azimuth) resulting in interferograms with 40 m pixel spacing. Sentinel-1's large swath width and short revisit time make it well suited for landscape-scale deformation monitoring. ASF HyP3 uses the 2021 release of the 30 m Copernicus "GLO-30" digital elevation model (DEM) product to remove the topographic component of the phase and geocode the interferograms [60]. The GLO-30 DEM product has an absolute vertical accuracy of <4 m (LE90) and an absolute horizontal accuracy of <6 m (CE90) [61], [62]. The DEM tiles covering the interferogram extents were geoid-corrected, resampled to match the pixel spacing of the interferograms, and reprojected to Universal Transverse Mercator (UTM) zone 13N [59]. The same output DEM products are used during CNN training.

### *B. Study Site*

We selected a study area in the Rocky Mountains in Colorado, USA (Figure 1) due to the large area above treeline and high density of slow-moving periglacial features [63]–[65]. The full ~46700 km$^2$ study area (including training, validation, and testing areas) contains, from north to south, the southern Front Range, the Gore Range, the northern Sawatch Range, the Mosquito Range, the Elk Mountains, the southern Sangre de Cristo Mountains, and the San Juan Mountains, offering a broad sample of mountain characteristics and an elevation range from ~1650-4400 m. The study area contains at least 2647 active rock glaciers with variable orientations covering a total of ~230 km$^2$ [64]. Median rock glacier area is 0.0579 ± 0.0975 km$^2$ and the median major and minor axis length of rock glacier polygons is 0.403 ± 0.306 km and 0.208 ± 0.118 km, respectively (± 1 standard deviation). While no previous studies considered the line-of-sight (LOS) InSAR velocity of Colorado rock glaciers, the mean LOS velocity of rock glaciers in the nearby Uinta Mountains ranged from ~0-3 cm/yr during the period from 2016 to 2019 [66]. The study area likely contains other slow-moving, coherent processes including non-rock glacier permafrost creep, solifluction, and landslide motion [e.g., 67].

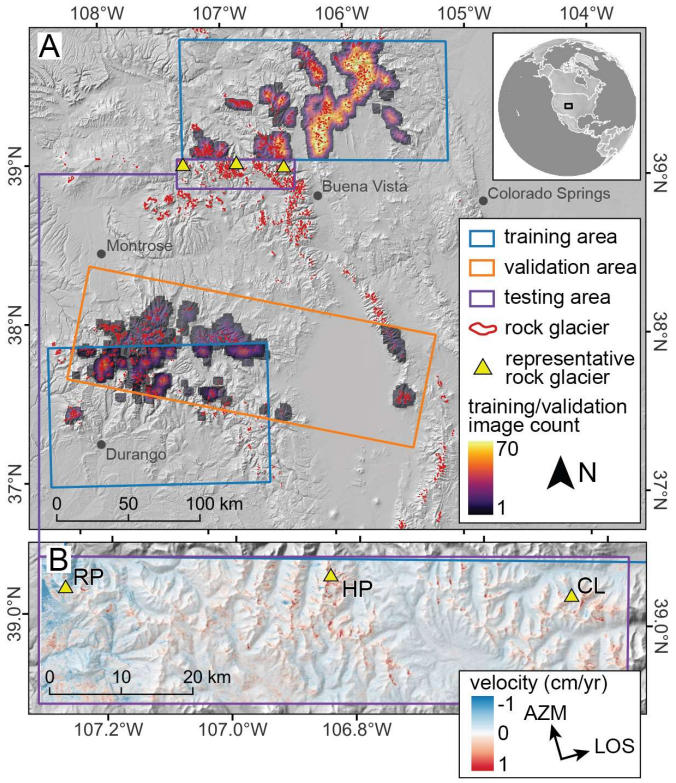


**Fig. 1.** Map showing training, validation, and testing area locations. Rock glacier inventory is from [64]. Yellow triangles in the testing area show locations of representative rock glaciers, which are, from west to east, Ragged Peak rock glacier (RP), Hayden Peak rock glacier (HP), and Crystal Lake rock glacier (CL). (a). Heatmap showing the spatial distribution of 128x128-pixel training and validation subsets. (b) Detail of the testing area, showing mean line-of-sight (LOS) velocity from the 7-year cumulative displacement time series for ascending Sentinel-1 pairs (Azimuth (AZM) and LOS directions shown in legend).

We selected three representative rock glaciers in the testing area for detailed kinematic analysis (Fig. 1, Table 1). The Crystal Lake rock glacier flows eastward from Ellingwood Ridge toward Crystal Lake Creek. The Ragged Peak rock glacier is part of a large rock glacier complex in the cirques between Ragged Peak to the west and an unnamed Ruby Range peak to the east. The Hayden Peak rock glacier occupies the valley between Hayden Peak to the north and South Hayden Peak to the south.

**Table 1.** Characteristics of selected representative rock glaciers.

| rock glacier name | location | area (km$^2$) | median elevation (m) | flow direction | uncorrected total displacement (cm) | CNN-corrected total displacement (cm) |
|---|---|---|---|---|---|---|
| Crystal Lake | 39.03528°, -106.45573° | 0.210 | 3561 | east | 6.7 | 6.6 |
| Ragged Peak | 39.03285°, -107.27372° | 0.082 | 3600 | north/northeast | 4.5 | 7.4 |
| Hayden Peak | 39.05568°, -106.84600° | 0.170 | 3834 | east/northeast | 6.9 | 6.2 |

## III. METHODS

### *A. Training Dataset Preparation*

We prepared training and validation datasets composed of 1) characteristic atmospheric noise maps and 2) characteristic displacement signal maps (Fig. 2). These maps were combined to form composite "training interferograms." During training, characteristic atmospheric noise maps serve as the "target noise" and corresponding characteristic displacement signal maps serve as the "target signal."

#### *Characteristic Atmospheric Noise Maps*

Extending the logic applied by Hanssen et al. [68], we assume that the magnitude of atmospheric noise far exceeds the line-of-sight magnitude of coherent periglacial displacement signals for short-baseline interferograms, and that apparent displacement is dominated by atmospheric noise. Assuming a mean rock glacier LOS displacement rate of 1 cm/yr [66], the mean (over all pixels) magnitude of atmospheric noise is on average 116 and 58 times greater than the magnitude of rock glacier displacement in all 6- and 12-day interferograms, respectively.

To prepare characteristic atmospheric noise maps, we processed all possible ascending and descending short temporal baseline Sentinel-1 interferograms (6- and 12-day) from June 15-October 15 of 2015-2022. This date range was selected to yield the maximum number of mostly snow-free interferograms. This process yielded 136 interferograms with a mean coverage of ~15,400 km$^2$ in the training areas and 45 interferograms with a mean coverage of ~19,800 km$^2$ in the validation area (Table 2; Supplemental Fig. 1). To eliminate residual apparent surface displacement signals, which are mostly caused by low coherence in areas with cliffs, vegetation, surface water, and snow, we used a 7x7-pixel gaussian filter with standard deviation of 5 pixels to smooth each interferogram.

**Table 2.** Summary of interferogram datasets.

| | product | location | flight direction | interferogram count | mean connections |
|---|---|---|---|---|---|
| training | target signal | north training area | ascending | 110 | 7.10 |
| | target noise | north training area | ascending | 50 | 1.72 |
| | target signal | north training area | descending | 137 | 7.41 |
| | target noise | north training area | descending | 45 | 1.76 |
| | target signal | south training area | ascending | 90 | 6.92 |
| | target noise | south training area | ascending | 41 | 1.71 |
| validation | target signal | validation area | descending | 84 | 7.00 |
| | target noise | validation area | descending | 45 | 1.76 |
| testing | testing interferograms | test area | ascending | 202 | 8.42 |

#### *Characteristic Displacement Signal Maps*

Characteristic displacement signal maps were derived from time series processing that produces low-noise mean displacement rate maps. We assume that the magnitude of 6 to 8-year LOS displacement signals for active periglacial features far exceeds the magnitude of atmospheric noise in these maps and that these maps can be used to approximate representative displacement rate signals. Following processing, each characteristic atmospheric noise map corresponds to one of four unique displacement rate maps, with a shared location and flight direction: ascending/north training area, descending/north training area, ascending/south training area, and descending/south validation area (Fig. 1).

To prepare each of our four LOS displacement signal maps, we created densely connected interferogram networks (Table 2; Supplemental Fig. 1) by processing ascending and descending Sentinel-1 interferogram pairs (temporal baselines from 6-60 days) from July 10-September 10 of 2015-2022, in addition to all interferogram pairs connecting the last three dates of a given year to each of the first three dates of the following year with data (200 total ascending interferograms, 221 total descending interferograms, mean of 7.14 interferograms created for a given acquisition). This date range was selected to include only maximally snow-free, high-coherence interferograms. The Miami INsar Time-series software in PYthon (MintPy) package [69] was used to perform time series inversion and produce mean LOS displacement rate maps. Before inversion, interferograms with mean coherence of <0.3 were removed, and after inversion, linear deramping and DEM error corrections were performed with MintPy. Time steps in the inverted time series fall on SAR image acquisition dates in the original interferogram network.

#### *Composite Training Interferogram Preparation*

The characteristic displacement signal and atmospheric noise maps were then subsetted, scaled, and combined to form composite training and validation interferograms. We used data collected along descending orbit 56 over the San Juan Mountains and the Sangre de Cristo Mountains for validation (Fig. 1A); all other data were used for training. While the validation area partially overlaps the training area in the San Juan Mountains, the interferograms used to create the validation dataset are independent of the interferograms used to create the training dataset. The overlap did not cause a problem in assessing CNN performance on unseen data, which is the primary purpose of the validation dataset.

To break the large atmospheric noise maps and corresponding displacement signal maps into smaller maps appropriate for training, we extracted a number of spatially matched subsets from both maps. For each map pair, we selected random 128 by 128-pixel subsets that satisfied the following conditions: 1) median elevation above 3300 m (approximately the lower bound for most rock glaciers in the study area), and 2) characteristic displacement signal dominated by coherent phase variation rather than white noise. To quantify the coherence of signals in the displacement map subsets, we first masked pixels with magnitude lower than the 99th percentile of the entire subset. For the remaining high-magnitude pixels, we calculated the mean cluster size (number of pixels that border one another). Larger mean cluster sizes indicate that high-magnitude pixels are adjacent, suggesting coherent displacement. We selected only subsets with a mean cluster size of 99th percentile magnitude displacement map pixels greater than three. For each acceptable subset pair, we extracted a spatially matching 128 by 128-pixel subset of the resampled Copernicus DEM output by HyP3. This random subsetting process was repeated until 11,215 training subset pairs and 1,704 validation subset pairs were generated, at which point it was stopped to limit redundancy in the datasets. Displacement signal subsets (output by MintPy in m/yr) were then scaled to produce a range of realistic displacement values

(in m). Displacement signal subsets were multiplied by a random scalar drawn from a lognormal distribution with a mean of -1.5 yr and a standard deviation of 1.5 yr. Scalars from this distribution ranged from ~0-35 yr.

The scaled displacement signal subsets (now in m) were then added to corresponding atmospheric noise subsets (in m) to create training and validation interferograms for a range of effective signal-to-noise ratios (SNRs, 0.000-40.26 with median of 0.034). Assuming a typical atmospheric noise magnitude of around 5-15 cm, this median SNR corresponds to a median target displacement signal magnitude of 0.17-0.51 cm. The scaled displacement subsets serve as the "target signal" for their respective training and validation interferograms.

*Data Normalization and Augmentation*

The training and validation interferograms and target signals were normalized between -1 and 1 using min-max normalization with shared parameters before they were supplied to the neural network. The minimum value across each interferogram/target signal pair served as the minimum, while the maximum value across the pair served as the maximum. Centering was performed by subtracting the median of the target signal from both the target signal and the training interferogram. The end result was that the target signal had a median of 0 and only the target noise remained when it was subtracted from the training interferogram. Each corresponding DEM subset was normalized between -1 and 1 using the minimum and maximum elevation values. The stacks of normalized training data (interferogram, target signal, and DEM) were randomly mirrored horizontally and vertically throughout training.

*B. Convolutional Neural Network Architecture*

We tested several CNN architectures, including the architecture developed by Rouet-Leduc et al. [58], and observed the best performance with ResDepth, a CNN with a U-Net architecture developed by Stucker & Schindler [70]. In addition to the skip connections typical of U-Nets, which add the outputs of encoder layers to the outputs of decoder layers at the same level, ResDepth includes an additional "outer" skip connection where the input image is added to the model output. Our implementation using PyTorch [71] had five downsampling and upsampling layers and two input channels: an interferogram and a corresponding DEM. It had 64 initial filters, increasing to a maximum of 512 filters, all of size 3 by 3 pixels. Batch normalization followed by rectified linear unit (ReLu) activation was performed after each convolutional layer except the final one. Our training sought to minimize the L1 loss between the model output and the target noise (training interferogram minus target signal). We used the AdamW optimizer [72], [73] with a learning rate of 0.0002, a weight decay of 0.02 and a batch size of 16. We trained for 150 epochs on a Nvidia T4 GPU.

*C. Alternative Correction Approaches*

We implemented two widely-used atmospheric noise corrections for comparison with the CNN results: a correction based on European Centre for Medium-Range Weather Forecasts (ECMWF) Reanalysis 5th Generation (ERA5) data [27] and high-pass filtering. High-pass filtering was performed by applying a gaussian blur with a kernel size of 25 pixels and a standard deviation of 3 pixels to the training or validation interferogram, then subtracting the blurred interferogram from the original. To perform the ERA5 correction we first used the pyaps3 package to predict atmospheric noise in each of our training and validation atmospheric noise maps. These ERA5 atmospheric noise prediction maps were subset alongside our atmospheric noise maps such that each 128 by 128-pixel interferogram had an accompanying ERA5 noise prediction. To set a local reference point for each ERA5 noise prediction, values in the noise prediction were shifted such that the noise prediction value at the location of the smallest magnitude target signal value matched the target noise value. The ERA5 correction was applied by subtracting the ERA5 noise prediction from the training or validation interferogram.

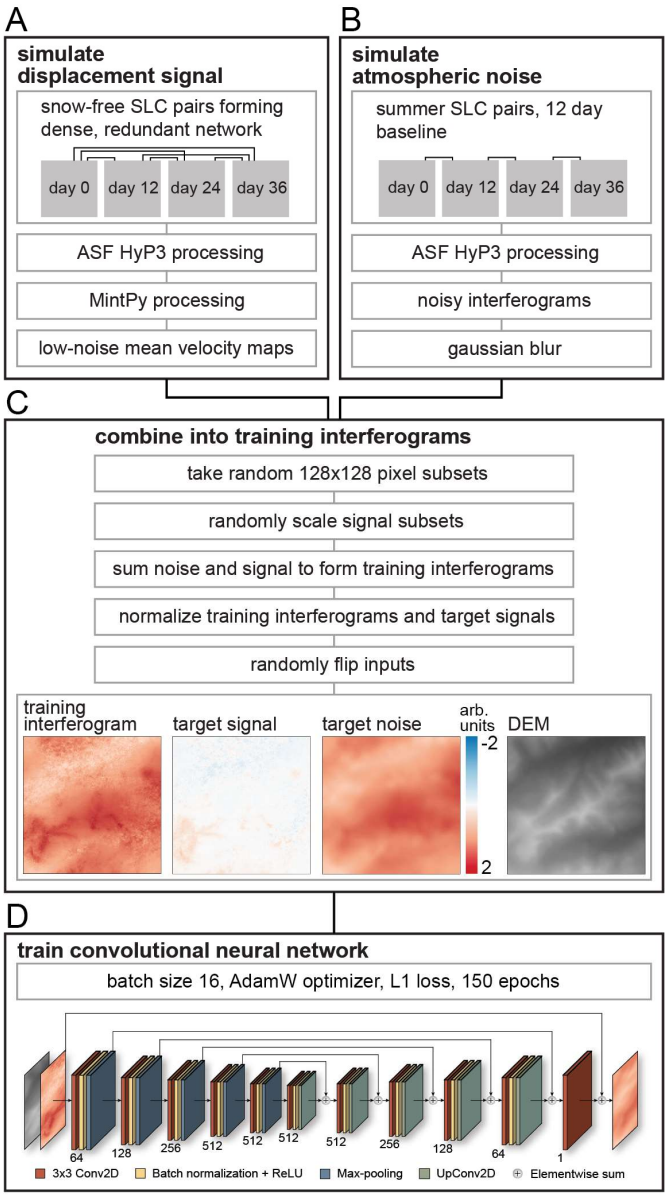


**Fig. 2.** Training flowchart. (a) Target displacement signal maps were simulated by inverting densely connected interferogram networks for time-dependent displacement, then calculating low-noise mean velocity maps. (b) Target atmospheric noise maps were simulated by blurring short temporal-baseline

interferograms, obscuring high-frequency signals. (c) Training interferograms were formed by summing scaled subsets of target displacement signal maps and target atmospheric noise maps. Training interferograms were then normalized and randomly flipped before training. (d) A U-Net CNN was trained to predict atmospheric noise, given input interferograms and accompanying DEMs. Neural network architecture and accompanying graphic modified from [70].

### *D. Evaluation*

We used the structural similarity index measure (SSIM) as implemented in the scikit-image package to compare the corrected training and validation interferograms to the corresponding target signal [74], [75]. The SSIM measures the perceptual similarity of two images on a scale between -1 and 1, where larger values correspond to a higher degree of similarity [74]. By comparing luminance, intensity, and contrast in a moving window, SSIM accounts for structural differences between images and is therefore a better metric of perceptual similarity than pixel-wise metrics such as mean squared error [74]. A Wilcoxon signed-rank test, which is nonparametric and paired, was used to establish significance of differences in prediction/target SSIMs between correction methods. A Kolmogorov–Smirnov test was used to determine whether SSIMs were normally distributed. A similar approach was used to evaluate the output maps from the high-pass filter and ERA5 correction approaches.

### *E. Testing*

#### *Testing Dataset Preparation*

We selected a testing area between the northern and southern training areas (Fig. 1). The Sawatch Range and Elk Mountains extend down from the northern training area into this testing area, providing an opportunity to assess CNN performance in unseen terrain that is similar to the terrain used in training. Our testing dataset was composed of a densely connected interferogram network created by processing all possible ascending Sentinel-1 interferograms with temporal baselines less than 60 days from July 1-September 30 of 2015-2022, in addition to all interferogram pairs connecting the last three dates of a given year to each of the first four dates of the following year (202 total interferograms; Table 2; Supplemental Fig. 1). This date range was selected to capture as much summer rock glacier displacement as possible before coherence was reduced by seasonal snow. As with training dataset preparation, interferograms and associated Copernicus DEM products were normalized between -1 and 1 using their respective minimum and maximum values.

#### *CNN Testing*

Each testing dataset (interferogram and DEM) was supplied to the trained CNN to generate a prediction of atmospheric noise. The noise prediction was subtracted from the testing interferogram, which was then denormalized. Time series inversion of the CNN-corrected interferogram network was performed with MintPy using the methods described in Section IIIA for displacement signal simulation. The same inversion process was repeated with the uncorrected interferogram network to prepare a control dataset.

To evaluate the CNN correction, we examined the cumulative LOS displacement time series for each of the three representative rock glaciers in the testing area. For each rock glacier, broadly flat, rocky, high-coherence, and nearby areas interpreted to be stable were selected as ‘reference areas’ and ‘stable areas,’ used to set a local reference point and to quantify remaining atmospheric noise, respectively. The distances between each rock glacier and corresponding reference areas and stable areas varied due to availability of appropriate terrain. At each acquisition date in our displacement time series, the median of apparent displacement in the reference area was subtracted from the displacement maps, effectively setting a stable local reference to mitigate landscape-scale atmospheric noise. To generate a rock glacier displacement time series, we computed the median value of pixels within the rock glacier polygon for each time step. We also computed the median of apparent displacement in nearby stable areas at each time step to provide an estimate of residual atmospheric noise and an estimate of uncertainty for the rock glacier displacement time series.

## IV. Results and Discussion

### *A. Training and Validation*

Following training, the CNN generated atmospheric noise predictions that matched the atmospheric noise in the input interferograms (“predicted noise” in Fig. 3A). When the predicted noise was subtracted from the training and validation interferograms, the remaining signals included: 1) high-frequency random noise over low-coherence vegetated and snow-covered areas with no observed bias, and 2) displacement signals with distinct edges over known periglacial features and landslides (“predicted signal” in Fig. 3A).

The alternative ERA5 and high-pass filter corrections did not perform as well as the CNN. The ERA5 correction appeared most effective when atmospheric noise was elevation-dependent. This result is expected, as the 31 km ERA5 grid cells are too large to resolve small-scale turbulent noise. Visually, the quality of the ERA5 correction was also sensitive to the choice of reference point location. The ERA5 correction results could likely be improved by manually picking a custom reference point for each interferogram, though this is impractical for large datasets with thousands of interferograms. In addition, the ERA5 correction approach frequently produced atmospheric noise predictions that did not resemble the observed atmospheric noise.

The high-pass filter correction was more effective for lower SNR values. For interferograms with higher SNRs, high-pass filtering tended to overpredict atmospheric noise (Supplemental Fig. 3). A high-pass filter correction could likely be improved by manually tuning the relevant parameters (e.g., kernel size) for each interferogram, but again, this is impractical for large datasets.

The mean SSIM computed between interferograms and corresponding target signals (hereafter, the “SSIM value” for a corrected dataset) for each correction varied slightly between epochs as the SNR of training and validation interferograms was randomly scaled. The distribution of training and validation SSIM values for all correction approaches was not normal (Fig. 3c, $p=0.00$, $n=11215$ subsets for training and $n=1704$ subsets

for validation). The CNN-corrected interferograms had the highest training and validation SSIM values, significantly larger than those for the ERA5-corrected (Fig. 3b; validation: p=0.00, n=1704) and high-pass filtered interferograms (p=0.00, n=1704). The CNN correction offered a 690% improvement in SSIM values over the ERA5 correction and a 209% improvement in SSIM values over high-pass filtering (Fig. 3C) for the validation dataset.

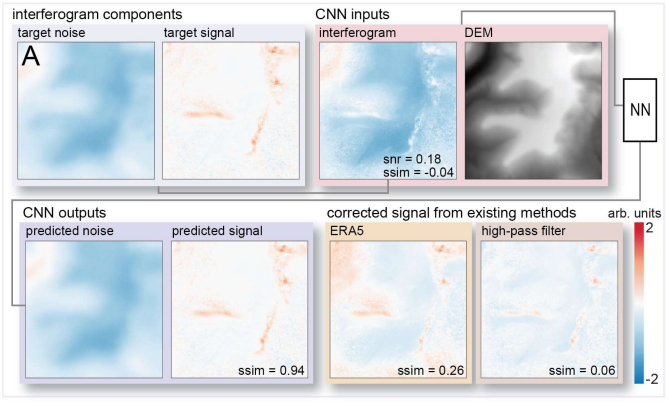


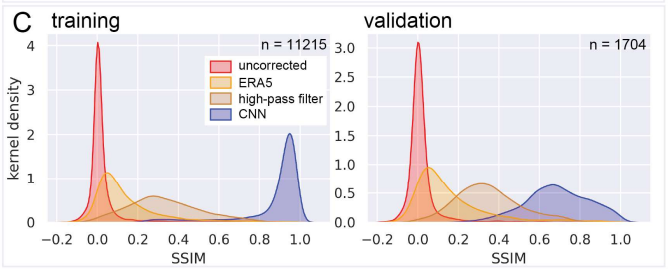


| D | median uncorrected SSIM | median CNN SSIM | median ERA5 SSIM | median low-pass filter SSIM |
|---|---|---|---|---|
| training | 0.002 ± 0.009 | 0.933 ± 0.031 | 0.093 ± 0.068 | 0.313 ± 0.119 |
| validation | 0.001 ± 0.009 | 0.682 ± 0.106 | 0.102 ± 0.074 | 0.331 ± 0.101 |

± corresponds to normalized median absolute deviation

**Fig. 3.** Training and validation results. (a) First row shows sample 128x128 pixel inputs for the CNN. Second row shows corresponding CNN outputs and comparable corrected signal from the ERA5 and high-pass filter correction methods. The CNN-corrected signal most closely resembles the target signal. (b) Scatterplot showing target vs. predicted signal for all pixels from the sample interferogram in A. The CNN-corrected signal has the smallest residuals. (c) Similarity of uncorrected and corrected interferograms to the target signal using the structural similarity index measure (SSIM) metric for all training and validation data. Higher SSIMs indicate greater similarity between interferograms and target signals. n corresponds to number of subsets. (d) Median and normalized median absolute deviation (NMAD) of the SSIM distributions shown in c. The CNN-corrected interferograms have the highest SSIMs and are most similar to the target signals.

The CNN correction has an advantage over the ERA5 and high-pass filtering corrections when applied to a large dataset, since it is adaptive and does not require parameter tuning to make realistic corrections for interferograms with differing noise and signal characteristics. In addition, the ERA5 correction is model-based and sometimes makes very inaccurate noise predictions compared to the observed noise in interferograms. However, CNN and high-pass filters are based purely on the observed data, and consequently tend to consistently reduce noise by deriving corrections from the data itself. Unlike the high-pass filter correction, the CNN filters out real displacement signals rather than simply blurring them, causing it to significantly outperform high-pass filtering, especially as SNR increases.

### *B. Testing*

As in training, our CNN produced noise predictions that matched the appearance of the real atmospheric noise for the test interferograms, including both elevation-dependent and turbulent noise (Fig. 4). Displacement signals spanning large areas (>10 km$^2$) were generally interpreted as atmospheric noise by the CNN, even where they had well-defined edges (Fig. 4A). Following time series processing, the uncorrected displacement time series contained apparent landscape-scale positive and negative LOS displacements, while the CNN-corrected time series contained a gradual accumulation of positive displacement signals over time (Fig. 4B). The magnitude of apparent km-scale displacement signals is lower in the CNN-corrected time series.

Our CNN interpreted negative signals (motion towards the satellite) as atmospheric noise more often than positive signals (motion away from the satellite). This was likely caused by infrequent movement of periglacial features towards the satellite in our training dataset, as features tend to flow downslope. While this issue could likely be alleviated by inverting the sign of the signal and noise in some portion of the training data, this may cause the CNN to learn unphysical relationships between topography, periglacial displacement signal, and the satellite LOS, ultimately decreasing the overall quality of the correction.

In some locations with short atmospheric noise length scales, like over mountain ridgelines, the CNN incorrectly interpreted atmospheric noise as a displacement signal. This issue is likely caused by blurring of the target noise prior to preparing the training and validation interferograms (Section IIIA), which was necessary to remove low-coherence signals and isolate the atmospheric component of the phase offset.

### *C. Rock Glacier Kinematics*

The median displacement time series for all rock glacier features show characteristic seasonal variability with higher velocities in the summer and lower velocities in the winter (Fig. 5) in both uncorrected and CNN-corrected records. Winter displacements show less variability in magnitude and direction in the CNN-corrected time series. For the Crystal Lake rock glacier and the Hayden Peak rock glacier, the cumulative uncorrected and CNN-corrected displacement was between 6.2 and 6.9 cm over the 7-year study period, corresponding to a mean displacement rate of ~1 cm/yr (Fig. 5A, C, Table 1). For the Ragged Peak rock glacier, the cumulative uncorrected

displacement is 4.5 cm, while the cumulative CNN-corrected displacement is 7.4 cm (Fig. 5B, Table 1). The uncorrected summer rock glacier displacements show apparent changes in LOS direction and spatial variability in displacement patterns from year to year (Fig. 6). The uncorrected displacements over summer stable areas were generally not close to zero and sometimes contained the same apparent changes in flow direction and velocity as the rock glacier time series, especially for Ragged Peak rock glacier (Fig. 6B), suggesting that local atmospheric noise contaminated the displacement signal.

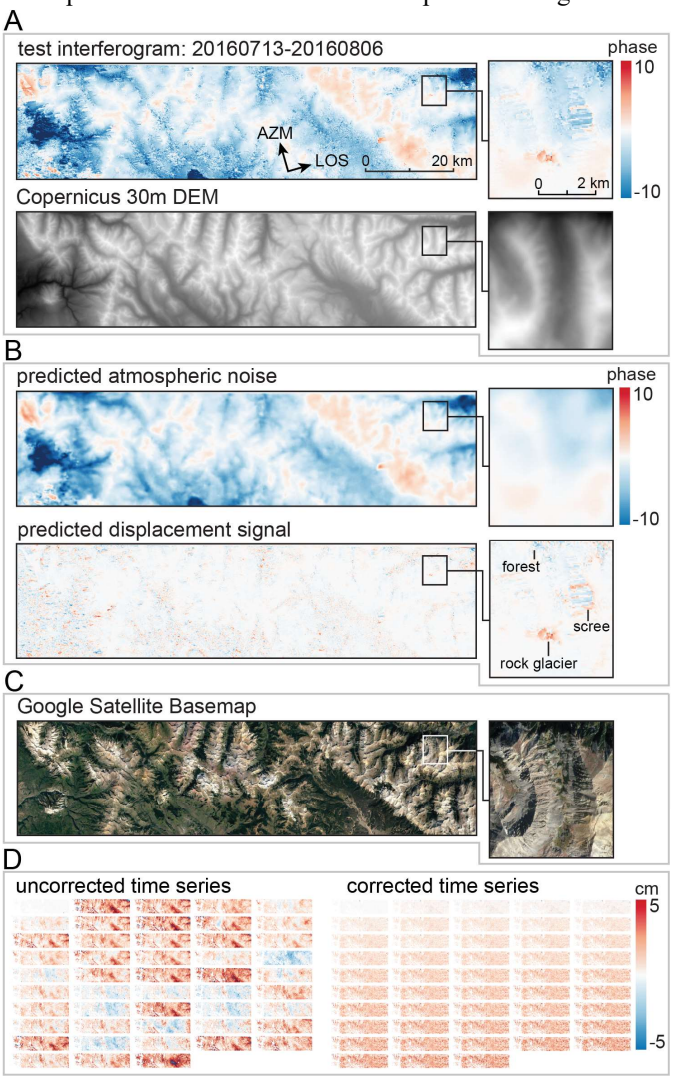


**Fig. 4.** Testing results. (a) Example CNN inputs for a test interferogram. The insets on the right show detail around the Crystal Lake rock glacier. (b) Example CNN output and corrected test interferogram. Note that kilometer-scale turbulent and stratified atmospheric noise is removed in the predicted displacement signal map, while the rock glacier displacement signal is preserved. (c) Google Satellite basemap for context. (d) Uncorrected (left) and CNN-corrected (right) cumulative displacement time series from inversion of the full 202 interferogram network used for testing. Note that the elevation-dependent atmospheric errors persist throughout the uncorrected cumulative displacement time series.

By comparison, the CNN-corrected time series displayed consistent summer motion in the downslope direction for all three rock glaciers. The Ragged Peak rock glacier appeared to flow towards the satellite (up and to the west) in the uncorrected time series and away from the satellite, in the expected downslope direction (down and to the east), in the CNN-corrected time series (Fig. 6B). This result demonstrates the ability of the CNN correction to capture the kinematic behavior of coherent, slow-moving surface features with high temporal resolution, even where there is significant atmospheric noise and limited reference areas in the immediate vicinity of these features. Displacement was near-zero with reduced variability over stable surfaces (Fig. 6B), indicating that the CNN correction effectively removed most atmospheric noise over stable areas.

### *D. Generalization*

We found that median SSIM values from training were consistently larger than median SSIM values from validation, suggesting that out-of-region generalization represents a challenge for the current CNN correction. This could likely be improved by 1) limiting to in-region training data; for example, training a network on Sawatch Range data from 2015-2019 and applying it to Sawatch Range data from 2020-2023, 2) increasing the coverage and diversity of terrain represented in the training data, and 3) further data augmentation and network architecture refinement. Generalization of CNNs in remote sensing is a widespread challenge and an area of ongoing research (e.g., [76]–[79]), and our correction approach will likely benefit from future work in these research areas.

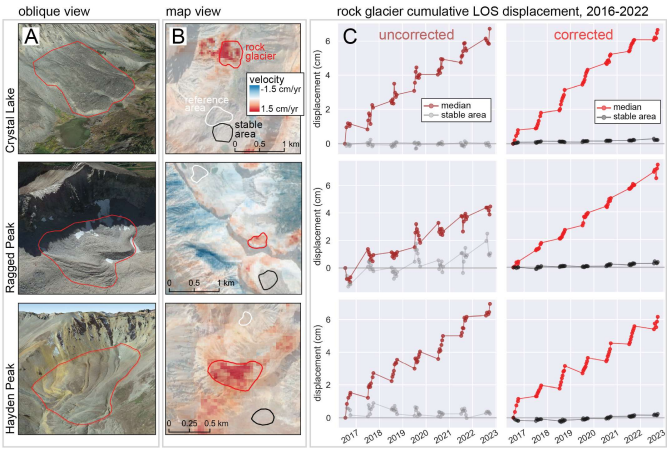


**Fig. 5.** Observed mean displacement rate and cumulative LOS displacement for three representative rock glaciers in the uncorrected and CNN-corrected time series spanning the 7-year period from 2016 to 2022. The cumulative displacement records are corrected using the median apparent displacement over a reference area (white outline) at each time step. Uncertainty is quantified using the displacement in the stable area. Note variability in the apparent displacement direction and magnitude over the stable area in the uncorrected time series (gray) compared to the CNN-corrected time series (black). The corrected rock glacier time series (bright red) contains summer and seasonal displacement patterns more consistent with the expected behavior of rock glaciers than the uncorrected time series (maroon).

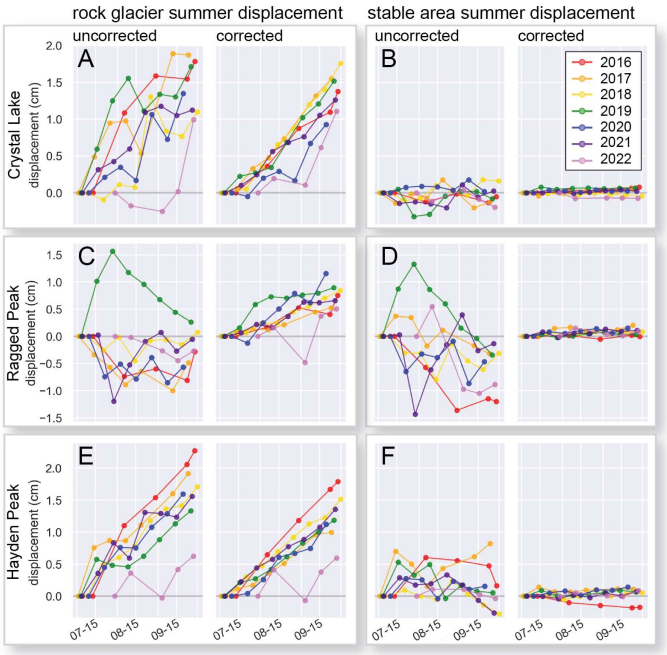


**Fig. 6.** Observed summer displacement of representative rock glaciers and stable areas in the uncorrected and CNN-corrected time series for the 7 years between 2016 and 2022. Displacement at the beginning of each summer period was set to zero. The uncorrected time series shows greater variability, and the apparent stable area displacement history is sometimes mirrored in the corresponding rock glacier displacement history. In the CNN-corrected time series, all rock glaciers move away from the satellite over time (as expected), with limited apparent stable area displacement.

### *E. Limitations and Future Work*

Our CNN correction is based on the differing spatial and topographic characteristics of atmospheric noise and slow-moving periglacial features. This approach involves two major assumptions.

The first assumption is that the true rock glacier displacement contribution to observed LOS phase offset is negligible in 6- and 12-day interferograms. This may not hold where InSAR is applied to detect faster displacements, like those associated with glaciers or earthquakes, which display significant phase offsets even in short-temporal baseline interferograms. However, atmospheric correction becomes less important in these high SNR cases, as standard time-series approaches applied to densely connected interferogram networks will effectively capture the kinematic behavior of fast-moving features.

The second assumption is that apparent displacement signals in the low-noise LOS displacement rate maps (the target signals during training) have fundamentally different spatial and topographic characteristics than the atmospheric noise. We expect the performance of our CNN correction to degrade as the spatial and topographic characteristics of the signal of interest approach those of the local atmospheric noise. Specifically, the CNN may interpret more true displacement signals as atmospheric noise, and vice versa.

As such, our current CNN correction approach is well-suited for features like smaller slow-moving landslides, stagnant debris-covered glaciers, rock glaciers, and ice-cored moraines. It is likely less appropriate for features spanning several kilometers with limited displacement signals, indistinct boundaries, and limited adjacent stable terrain (e.g., ice sheet interior). For example, elevation-dependent displacement signals related to inflation of volcanoes may appear visually similar to stratified atmospheric noise. We recommend that the dominant spatial wavelength of the atmospheric noise should be at least 2x the dominant spatial wavelength of the feature of interest for best results. Future efforts should systematically evaluate the effect of different pixel size, radar wavelength, acquisition geometry, and geographic location on the CNN correction performance.

Our CNN correction improved the accuracy of cumulative InSAR displacement measurements, removing apparent displacement in stable areas and correcting apparent rapid fluctuations in rock glacier displacement direction along the satellite LOS. Unfortunately, we did not have prior knowledge of the true 3D surface displacement vectors for any of the features of interest, which would provide independent validation for our displacement time series results. In the future, we hope to train and apply a similar CNN correction for landslides and rock glaciers with multiple years of in situ surface displacement measurements.

## V. Conclusion

We developed and implemented a statistical machine learning approach for correcting atmospheric noise in satellite interferometric synthetic aperture radar (InSAR) interferograms. We used on-demand InSAR processing and cloud computing resources to train, validate and test a denoising convolutional neural network (CNN) using simulated atmospheric noise and displacement signals derived from Sentinel-1 interferograms over the Rocky Mountains in Colorado, where slow-moving periglacial features above treeline are abundant. Our correction approach offers several advantages over existing techniques as it does not require external atmospheric data, is applied at the native spatial and temporal resolution of individual InSAR datasets, can correct both stratified and turbulent atmospheric noise, and was developed for use in challenging mountainous regions.

We found that our CNN correction significantly outperformed an ERA5 model-based correction and a high-pass filter correction, offering respective 690% and 209% improvements in structural similarity index measure (SSIM). We tested our approach by correcting a densely connected network of snow-free interferograms from the Sawatch Range, then inverting for time-dependent cumulative displacement. We found that the CNN-corrected displacement time series successfully removed atmospheric noise to reveal consistent and linear downslope summer displacement of three representative rock glaciers.

Our CNN correction relies on spatial and topographic differences between atmospheric noise and slow-moving displacement signals of interest. It is suitable for applications with 1) slow-moving features with negligible true displacement in short-baseline 6- and 12-day interferograms and 2) distinct spatial and topographic characteristics for features of interest and atmospheric noise. In these circumstances, our CNN

correction represents a step toward realizing the full potential of InSAR to monitor any coherent feature displacement with high spatial and temporal resolution and mm-scale accuracy. For alpine glaciers and periglacial features without in-situ instrumentation, the improved accuracy of CNN-corrected displacement measurements will allow us to better examine their short-term kinematics, improving our understanding of their dynamics and ongoing response to climate change.

## ACKNOWLEDGMENT

G. Brencher acknowledges Eric Gagliano and Bareera Mirza, who collaborated on the class project that inspired this work. The authors acknowledge Dr. Alexander Handwerger, Dr. Gregoire Guillet, and Seth Vanderwilt for their helpful feedback at various points throughout the methods development process.

## REFERENCES

[1] R. Bürgmann, P. A. Rosen, and E. J. Fielding, "Synthetic Aperture Radar Interferometry to Measure Earth's Surface Topography and Its Deformation," *Annu. Rev. Earth Planet. Sci.*, vol. 28, no. 1, pp. 169–209, 2000, doi: 10.1146/annurev.earth.28.1.169.

[2] D. Massonnet and K. L. Feigl, "Radar interferometry and its application to changes in the Earth's surface," *Rev. Geophys.*, vol. 36, no. 4, pp. 441–500, 1998, doi: 10.1029/97RG03139.

[3] P. A. Rosen *et al.*, "Synthetic aperture radar interferometry," *Proc. IEEE*, vol. 88, no. 3, pp. 333–382, Mar. 2000, doi: 10.1109/5.838084.

[4] H. A. Zebker, P. A. Rosen, and S. Hensley, "Atmospheric effects in interferometric synthetic aperture radar surface deformation and topographic maps," *J. Geophys. Res. Solid Earth*, vol. 102, no. B4, pp. 7547–7563, 1997, doi: 10.1029/96JB03804.

[5] C. Delacourt, P. Briole, and J. A. Achache, "Tropospheric corrections of SAR interferograms with strong topography. Application to Etna," *Geophys. Res. Lett.*, vol. 25, no. 15, pp. 2849–2852, 1998, doi: 10.1029/98GL02112.

[6] D. Remy, Y. Chen, J. L. Froger, S. Bonvalot, L. Cordoba, and J. Fustos, "Revised interpretation of recent InSAR signals observed at Llaima volcano (Chile)," *Geophys. Res. Lett.*, vol. 42, no. 10, pp. 3870–3879, 2015, doi: 10.1002/2015GL063872.

[7] D. Loibl, B. Bookhagen, S. Valade, and C. Schneider, "OSARIS, the 'Open Source SAR Investigation System' for Automatized Parallel InSAR Processing of Sentinel-1 Time Series Data With Special Emphasis on Cryosphere Applications," *Front. Earth Sci.*, vol. 7, 2019, Accessed: Feb. 06, 2023. [Online]. Available: https://www.frontiersin.org/articles/10.3389/feart.2019.00172

[8] M. Eineder, "Problems and Solutions for InSAR Digital Elevation Model Generation of Mountainous Terrain," vol. 550, p. 18, Jun. 2004.

[9] C. Colesanti and J. Wasowski, "Investigating landslides with space-borne Synthetic Aperture Radar (SAR) interferometry," *Eng. Geol.*, vol. 88, no. 3, pp. 173–199, Dec. 2006, doi: 10.1016/j.enggeo.2006.09.013.

[10] S. Grebby *et al.*, "Remote Monitoring of Ground Motion Hazards in High Mountain Terrain Using InSAR: A Case Study of the Lake Sarez Area, Tajikistan," *Appl. Sci.*, vol. 11, no. 18, Art. no. 18, Jan. 2021, doi: 10.3390/app11188738.

[11] M. Huss *et al.*, "Toward mountains without permanent snow and ice," *Earths Future*, vol. 5, no. 5, pp. 418–435, 2017, doi: 10.1002/2016EF000514.

[12] A. Dehecq *et al.*, "Twenty-first century glacier slowdown driven by mass loss in High Mountain Asia," *Nat. Geosci.*, vol. 12, no. 1, Art. no. 1, Jan. 2019, doi: 10.1038/s41561-018-0271-9.

[13] R. Delaloye, C. Lambiel, and I. Gärtner-Roer, "Overview of rock glacier kinematics research in the Swiss Alps," *Geogr. Helvetica*, vol. 65, no. 2, pp. 135–145, Jun. 2010, doi: 10.5194/gh-65-135-2010.

[14] L. Ravanel, P.-A. Duvillard, M. Jaboyedoff, and C. Lambiel, "Recent evolution of an ice-cored moraine at the Gentianes Pass, Valais Alps, Switzerland," *Land Degrad. Dev.*, vol. 29, no. 10, pp. 3693–3708, 2018, doi: 10.1002/ldr.3088.

[15] M. Stoffel and C. Huggel, "Effects of climate change on mass movements in mountain environments," *Prog. Phys. Geogr. Earth Environ.*, vol. 36, no. 3, pp. 421–439, Jun. 2012, doi: 10.1177/0309133312441010.

[16] D. P. S. Bekaert, R. J. Walters, T. J. Wright, A. J. Hooper, and D. J. Parker, "Statistical comparison of InSAR tropospheric correction techniques," *Remote Sens. Environ.*, vol. 170, pp. 40–47, Dec. 2015, doi: 10.1016/j.rse.2015.08.035.

[17] X. Ding, Z. Li, J. Zhu, G. Feng, and J. Long, "Atmospheric Effects on InSAR Measurements and Their Mitigation," *Sensors*, vol. 8, no. 9, Art. no. 9, Sep. 2008, doi: 10.3390/s8095426.

[18] T. R. Emardson, M. Simons, and F. H. Webb, "Neutral atmospheric delay in interferometric synthetic aperture radar applications: Statistical description and mitigation," *J. Geophys. Res. Solid Earth*, vol. 108, no. B5, 2003, doi: 10.1029/2002JB001781.

[19] R. B. Lohman and M. Simons, "Some thoughts on the use of InSAR data to constrain models of surface deformation: Noise structure and data downsampling," *Geochem. Geophys. Geosystems*, vol. 6, no. 1, 2005, doi: 10.1029/2004GC000841.

[20] Z. W. Li, X. L. Ding, C. Huang, Z. R. Zou, and Y. L. Chen, "Atmospheric effects on repeat-pass InSAR measurements over Shanghai region," *J. Atmospheric Sol.-Terr. Phys.*, vol. 69, no. 12, pp. 1344–1356, Aug. 2007, doi: 10.1016/j.jastp.2007.04.007.

[21] K. D. Murray, D. P. S. Bekaert, and R. B. Lohman, "Tropospheric corrections for InSAR: Statistical assessments and applications to the Central United States and Mexico," *Remote Sens. Environ.*, vol. 232, p. 111326, Oct. 2019, doi: 10.1016/j.rse.2019.111326.

[22] R. Hanssen and A. Feijt, "a First Quantitative Evaluation of Atmospheric Effects on SAR Interferometry," vol. 406, p. 277, Mar. 1997.

[23] V. Janssen, L. Ge, and C. Rizos, "Tropospheric corrections to SAR interferometry from GPS observations," *GPS Solut.*, vol. 8, no. 3, pp. 140–151, Sep. 2004, doi: 10.1007/s10291-004-0099-1.

[24] Z. Li, E. J. Fielding, P. Cross, and J.-P. Muller, "Interferometric synthetic aperture radar atmospheric correction: GPS topography-dependent turbulence model," *J. Geophys. Res. Solid Earth*, vol. 111, no. B2, 2006, doi: 10.1029/2005JB003711.

[25] C. Yu, Z. Li, and N. T. Penna, "Interferometric synthetic aperture radar atmospheric correction using a GPS-based iterative tropospheric decomposition model," *Remote Sens. Environ.*, vol. 204, pp. 109–121, Jan. 2018, doi: 10.1016/j.rse.2017.10.038.

[26] M.-P. Doin, C. Lasserre, G. Peltzer, O. Cavalié, and C. Doubre, "Corrections of stratified tropospheric delays in SAR interferometry: Validation with global atmospheric models," *J. Appl. Geophys.*, vol. 69, no. 1, pp. 35–50, Sep. 2009, doi: 10.1016/j.jappgeo.2009.03.010.

[27] R. Jolivet, R. Grandin, C. Lasserre, M.-P. Doin, and G. Peltzer, "Systematic InSAR tropospheric phase delay corrections from global meteorological reanalysis data," *Geophys. Res. Lett.*, vol. 38, no. 17, 2011, doi: 10.1029/2011GL048757.

[28] R. Jolivet *et al.*, "Improving InSAR geodesy using Global Atmospheric Models," *J. Geophys. Res. Solid Earth*, vol. 119, no. 3, pp. 2324–2341, 2014, doi: 10.1002/2013JB010588.

[29] J. Foster, B. Brooks, T. Cherubini, C. Shacat, S. Businger, and C. L. Werner, "Mitigating atmospheric noise for InSAR using a high resolution weather model," *Geophys. Res. Lett.*, vol. 33, no. 16, 2006, doi: 10.1029/2006GL026781.

[30] L. Shen, A. Hooper, and J. Elliott, "A Spatially Varying Scaling Method for InSAR Tropospheric Corrections Using a High-Resolution Weather Model," *J. Geophys. Res. Solid Earth*, vol. 124, no. 4, pp. 4051–4068, 2019, doi: 10.1029/2018JB016189.

[31] Z. Li, J. -P. Muller, P. Cross, P. Albert, J. Fischer, and R. Bennartz, "Assessment of the potential of MERIS near-infrared water vapour products to correct ASAR interferometric measurements," *Int. J. Remote Sens.*, vol. 27, no. 2, pp. 349–365, Jan. 2006, doi: 10.1080/01431160500307342.

[32] Z. Li, E. J. Fielding, P. Cross, and J.-P. Muller, "Interferometric synthetic aperture radar atmospheric correction: Medium Resolution Imaging Spectrometer and Advanced Synthetic Aperture Radar integration," *Geophys. Res. Lett.*, vol. 33, no. 6, 2006, doi: 10.1029/2005GL025299.

[33] Y. Gao, L. Xiao, D. Chen, J. Xu, and H. Zhang, "Comparison between past and future extreme precipitations simulated by global and regional climate models over the Tibetan Plateau," *Int. J. Climatol.*, vol. 38, no. 3, pp. 1285–1297, 2018, doi: 10.1002/joc.5243.

[34] S. Jain, S. K. Mishra, P. Salunke, and S. Sahany, "Importance of the resolution of surface topography vis-à-vis atmospheric and surface processes in the simulation of the climate of Himalaya-Tibet highland," *Clim. Dyn.*, vol. 52, no. 7, pp. 4735–4748, Apr. 2019, doi: 10.1007/s00382-018-4411-0.

[35] A. Hamm *et al.*, "Intercomparison of Gridded Precipitation Datasets over a Sub-Region of the Central Himalaya and the Southwestern Tibetan Plateau," *Water*, vol. 12, no. 11, Art. no. 11, Nov. 2020, doi: 10.3390/w12113271.

[36] W. Gong, F. Meyer, P. W. Webley, D. Morton, and S. Liu, "Performance analysis of atmospheric correction in InSAR data based on the Weather Research and Forecasting Model (WRF)," in *2010 IEEE International Geoscience and Remote Sensing Symposium*, Jul. 2010, pp. 2900–2903. doi: 10.1109/IGARSS.2010.5652267.

[37] F. Beauducel, P. Briole, and J.-L. Froger, "Volcano-wide fringes in ERS synthetic aperture radar interferograms of Etna (1992–1998): Deformation or tropospheric effect?," *J. Geophys. Res. Solid Earth*, vol. 105, no. B7, pp. 16391–16402, 2000, doi: 10.1029/2000JB900095.

[38] D. P. S. Bekaert, A. Hooper, and T. J. Wright, "A spatially variable power law tropospheric correction technique for InSAR data," *J. Geophys. Res. Solid Earth*, vol. 120, no. 2, pp. 1345–1356, 2015, doi: 10.1002/2014JB011558.

[39] A. Ferretti, C. Prati, and F. Rocca, "Multibaseline InSAR DEM reconstruction: the wavelet approach," *IEEE Trans. Geosci. Remote Sens.*, vol. 37, no. 2, pp. 705–715, Mar. 1999, doi: 10.1109/36.752187.

[40] H. Zebker, "Accuracy of a Model-Free Algorithm for Temporal InSAR Tropospheric Correction," *Remote Sens.*, vol. 13, no. 3, Art. no. 3, Jan. 2021, doi: 10.3390/rs13030409.

[41] V. Jain and S. Seung, "Natural Image Denoising with Convolutional Networks," in *Advances in Neural Information Processing Systems*, Curran Associates, Inc., 2008. Accessed: Feb. 06, 2023. [Online]. Available: https://proceedings.neurips.cc/paper/2008/hash/c16a5320fa475530d9583c34fd356ef5-Abstract.html

[42] L. Gondara, "Medical Image Denoising Using Convolutional Denoising Autoencoders," in *2016 IEEE 16th International Conference on Data Mining Workshops (ICDMW)*, Dec. 2016, pp. 241–246. doi: 10.1109/ICDMW.2016.0041.

[43] A. E. Ilesanmi and T. O. Ilesanmi, "Methods for image denoising using convolutional neural network: a review," *Complex Intell. Syst.*, vol. 7, no. 5, pp. 2179–2198, Oct. 2021, doi: 10.1007/s40747-021-00428-4.

[44] S. Mukherjee, A. Zimmer, N. K. Kottayil, X. Sun, P. Ghuman, and I. Cheng, "CNN-Based InSAR Denoising and Coherence Metric," in *2018 IEEE SENSORS*, Oct. 2018, pp. 1–4. doi: 10.1109/ICSENS.2018.8589920.

[45] W. Yang, Y. He, S. Yao, L. Zhang, S. Cao, and Z. Wen, "An InSAR Interferogram Filtering Method Based on Multi-Level Feature Fusion CNN," *Sensors*, vol. 22, no. 16, Art. no. 16, Jan. 2022, doi: 10.3390/s22165956.

[46] S. Vitale, G. Ferraioli, and V. Pascazio, "A CNN Based Solution for InSAR Phase Denoising," in *IGARSS 2022 - 2022 IEEE International Geoscience and Remote*

*Sensing Symposium*, Jul. 2022, pp. 931–934. doi: 10.1109/IGARSS46834.2022.9883956.

[47] Z. Wu, H. Zhang, Y. Wang, T. Wang, and R. Wang, "A Deep Learning Based Method for Local Subsidence Detection and InSAR Phase Unwrapping: Application to Mining Deformation Monitoring," in *IGARSS 2020 - 2020 IEEE International Geoscience and Remote Sensing Symposium*, Sep. 2020, pp. 20–23. doi: 10.1109/IGARSS39084.2020.9323342.

[48] F. Sica, F. Calvanese, G. Scarpa, and P. Rizzoli, "A CNN-Based Coherence-Driven Approach for InSAR Phase Unwrapping," *IEEE Geosci. Remote Sens. Lett.*, vol. 19, pp. 1–5, 2022, doi: 10.1109/LGRS.2020.3029565.

[49] O. M. Sorkhabi, A. S. Nejad, and M. Khajehzadeh, "Evaluation of Isfahan City Subsidence Rate Using InSAR and Artificial Intelligence," *KSCE J. Civ. Eng.*, vol. 26, no. 6, pp. 2901–2908, Jun. 2022, doi: 10.1007/s12205-022-2013-1.

[50] C. P. Schwegmann, W. Kleynhans, J. Engelbrecht, L. W. Mdakane, and R. G. V. Meyer, "Subsidence feature discrimination using deep convolutional neural networks in synthetic aperture radar imagery," in *2017 IEEE International Geoscience and Remote Sensing Symposium (IGARSS)*, Jul. 2017, pp. 4626–4629. doi: 10.1109/IGARSS.2017.8128031.

[51] N. Anantrasirichai *et al.*, "Detecting Ground Deformation in the Built Environment Using Sparse Satellite InSAR Data With a Convolutional Neural Network," *IEEE Trans. Geosci. Remote Sens.*, vol. 59, no. 4, pp. 2940–2950, Apr. 2021, doi: 10.1109/TGRS.2020.3018315.

[52] N. Anantrasirichai, J. Biggs, F. Albino, P. Hill, and D. Bull, "Application of Machine Learning to Classification of Volcanic Deformation in Routinely Generated InSAR Data," *J. Geophys. Res. Solid Earth*, vol. 123, no. 8, pp. 6592–6606, 2018, doi: 10.1029/2018JB015911.

[53] N. Anantrasirichai, J. Biggs, F. Albino, and D. Bull, "The Application of Convolutional Neural Networks to Detect Slow, Sustained Deformation in InSAR Time Series," *Geophys. Res. Lett.*, vol. 46, no. 21, pp. 11850–11858, 2019, doi: 10.1029/2019GL084993.

[54] J. Wang *et al.*, "Generalizing to Unseen Domains: A Survey on Domain Generalization," *IEEE Trans. Knowl. Data Eng.*, pp. 1–1, 2022, doi: 10.1109/TKDE.2022.3178128.

[55] Y. Liu *et al.*, "Study of the Automatic Recognition of Landslides by Using InSAR Images and the Improved Mask R-CNN Model in the Eastern Tibet Plateau," *Remote Sens.*, vol. 14, no. 14, Art. no. 14, Jan. 2022, doi: 10.3390/rs14143362.

[56] C. M. J. Brengman and W. D. Barnhart, "Identification of Surface Deformation in InSAR Using Machine Learning," *Geochem. Geophys. Geosystems*, vol. 22, no. 3, p. e2020GC009204, 2021, doi: 10.1029/2020GC009204.

[57] C. Chen *et al.*, "Removing InSAR Topography-Dependent Atmospheric Effect Based on Deep Learning," *Remote Sens.*, vol. 14, no. 17, Art. no. 17, Jan. 2022, doi: 10.3390/rs14174171.

[58] B. Rouet-Leduc, R. Jolivet, M. Dalaison, P. A. Johnson, and C. Hulbert, "Autonomous extraction of millimeter-scale deformation in InSAR time series using deep learning," *Nat. Commun.*, vol. 12, no. 1, Art. no. 1, Nov. 2021, doi: 10.1038/s41467-021-26254-3.

[59] K. Hogenson *et al.*, "Hybrid Pluggable Processing Pipeline (HyP3): A cloud-native infrastructure for generic processing of SAR data." Zenodo, Feb. 15, 2023. doi: 10.5281/zenodo.7644424.

[60] European Space Agency, "Copernicus Digital Elevation Model (DEM)." 2021. [Online]. Available: https://registry.opendata.aws/copernicus-dem/

[61] NSDDA, "Geospatial positioning accuracy standards part 3: National standard for spatial data accuracy (no. FGDC-STD-007.3-1998)." 1998.

[62] European Space Agency, "Copernicus DEM Product Handbook." Jun. 03, 2022. [Online]. Available: https://spacedata.copernicus.eu/documents/20123/121239/GEO1988-CopernicusDEM-SPE-002_ProductHandbook_I4.0.pdf/92df0801-6714-20e4-75ae-0be634b9e301?t=1666775307957

[63] J. R. Janke, "Long-Term Flow Measurements (1961-2002) of the Arapaho, Taylor, and Fair Rock Glaciers, Front Range, Colorado," *Phys. Geogr.*, vol. 26, no. 4, pp. 313–336, Jan. 2005, doi: 10.2747/0272-3646.26.4.313.

[64] G. Johnson, H. Chang, and A. Fountain, "Active rock glaciers of the contiguous United States: geographic information system inventory and spatial distribution patterns," *Earth Syst. Sci. Data*, vol. 13, no. 8, pp. 3979–3994, Aug. 2021, doi: 10.5194/essd-13-3979-2021.

[65] A. Routt, "An Investigation of Intra-Annual Flow Rates of a Rock Glacier in the San Juan Mountains of Southwest Colorado," M.A., University of Colorado Colorado Springs, United States -- Colorado, 2022. Accessed: Feb. 06, 2023. [Online]. Available: https://www.proquest.com/docview/2669075978/abstract/DC8C150AE61448EPQ/1

[66] G. Brencher, A. L. Handwerger, and J. S. Munroe, "InSAR-based characterization of rock glacier movement in the Uinta Mountains, Utah, USA," *The Cryosphere*, vol. 15, no. 10, pp. 4823–4844, Oct. 2021, doi: 10.5194/tc-15-4823-2021.

[67] B. B. Mirus *et al.*, "Landslides across the USA: occurrence, susceptibility, and data limitations," *Landslides*, vol. 17, no. 10, pp. 2271–2285, Oct. 2020, doi: 10.1007/s10346-020-01424-4.

[68] R. F. Hanssen, T. M. Weckwerth, H. A. Zebker, and R. Klees, "High-Resolution Water Vapor Mapping from Interferometric Radar Measurements," *Science*, vol. 283, no. 5406, pp. 1297–1299, Feb. 1999, doi: 10.1126/science.283.5406.1297.

[69] Z. Yunjun, H. Fattahi, and F. Amelung, "Small baseline InSAR time series analysis: Unwrapping error correction and noise reduction," *Comput. Geosci.*, vol. 133, p. 104331, Dec. 2019, doi: 10.1016/j.cageo.2019.104331.

[70] C. Stucker and K. Schindler, “ResDepth: A deep residual prior for 3D reconstruction from high-resolution satellite images,” *ISPRS J. Photogramm. Remote Sens.*, vol. 183, pp. 560–580, Jan. 2022, doi: 10.1016/j.isprsjprs.2021.11.009.

[71] A. Paszke *et al.*, “PyTorch: An Imperative Style, High-Performance Deep Learning Library,” in *Advances in Neural Information Processing Systems*, Curran Associates, Inc., 2019. Accessed: Feb. 06, 2023. [Online]. Available: https://proceedings.neurips.cc/paper/2019/hash/bdbca288fee7f92f2bfa9f7012727740-Abstract.html

[72] D. P. Kingma and J. Ba, “Adam: A Method for Stochastic Optimization.” arXiv, Jan. 29, 2017. doi: 10.48550/arXiv.1412.6980.

[73] I. Loshchilov and F. Hutter, “Decoupled Weight Decay Regularization.” arXiv, Jan. 04, 2019. doi: 10.48550/arXiv.1711.05101.

[74] Z. Wang, A. C. Bovik, H. R. Sheikh, and E. P. Simoncelli, “Image quality assessment: from error visibility to structural similarity,” *IEEE Trans. Image Process.*, vol. 13, no. 4, pp. 600–612, Apr. 2004, doi: 10.1109/TIP.2003.819861.

[75] S. van der Walt *et al.*, “scikit-image: image processing in Python,” *PeerJ*, vol. 2, p. e453, Jun. 2014, doi: 10.7717/peerj.453.

[76] V. Mnih, “Machine Learning for Aerial Image Labeling,” Ph.D., University of Toronto (Canada), Canada -- Ontario, CA, 2013. Accessed: Mar. 10, 2023. [Online]. Available: https://www.proquest.com/docview/1500835065/abstract/111B3DE9FC6E456FPQ/1

[77] E. Maggiori, Y. Tarabalka, G. Charpiat, and P. Alliez, “Can semantic labeling methods generalize to any city? the inria aerial image labeling benchmark,” in *2017 IEEE International Geoscience and Remote Sensing Symposium (IGARSS)*, Jul. 2017, pp. 3226–3229. doi: 10.1109/IGARSS.2017.8127684.

[78] T. Gong, X. Zheng, and X. Lu, “Cross-Domain Scene Classification by Integrating Multiple Incomplete Sources,” *IEEE Trans. Geosci. Remote Sens.*, vol. 59, no. 12, pp. 10035–10046, Dec. 2021, doi: 10.1109/TGRS.2020.3034344.

[79] M. Ahmad, M. Mazzara, and S. Distefano, “Regularized CNN Feature Hierarchy for Hyperspectral Image Classification,” *Remote Sens.*, vol. 13, no. 12, Art. no. 12, Jan. 2021, doi: 10.3390/rs13122275.